

## ARTICLE OPEN

## Mechanism of surface uranium hydride formation during corrosion of uranium

Hefei Ji<sup>1</sup>, Haoxi Wu<sup>1</sup>, Qifa Pan<sup>2</sup>, Dingzhou Cai<sup>1</sup>, Xiandong Meng<sup>1</sup>, Xianglin Chen<sup>1</sup>, Peng Shi<sup>1</sup> and Xiaolin Wang<sup>1</sup>

Uranium is widely used in the nuclear industry and it is well known that uranium hydride, UH<sub>3</sub>, forms when uranium is exposed to air. The associated volume change during this transition can cause the surface region to crack, compromising structural integrity. Here, hydriding regions beneath hydride surface craters are studied by secondary ion mass spectroscopy (SIMS) and X-ray photoelectron spectroscopy (XPS). Our results indicate that strain transition regions exist, which are induced by hydrogen with a certain thickness between hydride craters and the uranium bulk. The SIMS and XPS results suggest that hydrogen exists covalently with uranium and oxygen in these transition regions. A micro-scale induction period model based on the transition region and previous hydriding models is developed. Within the so-called micro-scale induction period, hydrogen diffuses and accumulates at particular sites before reaching the critical concentration required to form stoichiometric UH<sub>3</sub> in the transition regions.

*npj Materials Degradation* (2019)3:9; <https://doi.org/10.1038/s41529-019-0073-6>

## INTRODUCTION

Uranium hydride (UH<sub>3</sub>), a radioactive intermediate-level waste material with pyrophoricity when exposed to air, is an unwanted corrosion product of metallic uranium (U). Moreover, because of the difference in density between the metallic U (19.1 g/cm<sup>3</sup>) and hydride (10.95 g/cm<sup>3</sup>), the regional attack of hydrogen results in robust volume expansion underneath the oxide at the metal-oxide interface. The volume expansion breaks open the overlayer, reduces the surface integrity and even leads to material failure. Hence, U hydrogenation problems have been generally studied in the past several decades. The reaction between U and H are widely accepted to be governed by four stages: the induction period, nucleation and growth period, bulk reaction, and termination period.<sup>1,2</sup> The first two are thought to be the key periods, during which H aggregates and hydride sites nucleate and grow. In the induction period, hydrogen penetrates the surface passivation layer of oxide then gathers at the oxide-metal interface. For the nucleation and growth period, once the hydride nucleated and subsequently grew, because of the volume expansion the surface oxide layer will be broken through, meanwhile hydrogen keeps on penetrating into and reacting with the bulk material. The hydride sites always grow along the surface and into the bulk with the progression of the reaction front to form discrete hydride craters.

Hydriding pitting locations have been one of the key concerned issues of many studies.<sup>1,3–7</sup> Previous work indicates that, the H solubility limit in  $\alpha$ -U at room temperature (293 K, 20 °C) and 1-atm pressure is approximately 0.04 wppm (weight parts per million, 1  $\mu$ g/g).<sup>8</sup> The critical concentration required to form stoichiometric UH<sub>3</sub> throughout the metal bulk is approximately 12,700 wppm,<sup>9</sup> being six orders of magnitude higher than the dissolved H concentration. Therefore, UH<sub>3</sub> transformation must occur locally rather than uniformly across the surface, under conditions in which the dissolved H atoms can accumulate and exceed the

critical concentration at isolated locations. Thus, H-induced U corrosion follows a localized, spatially heterogeneous, and random pattern of hydride initiation.<sup>3,4,10,11</sup> Metallic U is in the orthorhombic  $\alpha$ -phase with significant anisotropy, and the bulk material contains many defects including macro-scale inclusions and micro-scale boundaries, vacancies, and impurities. Investigations of H-induced metallic U corrosion and its alloys have provided evidences that each of the above-mentioned defect types provides a corrosion initiation site for hydride.<sup>1,5,6,12,13</sup> Electron backscatter diffraction (EBSD) has been utilized by Bingert et al.<sup>5</sup> to prove the significant finding that grain and twin boundaries strongly influence initial hydride site locations.<sup>14</sup> Harker et al.<sup>15</sup> have found that inclusions have an effect on the initial location of the H attacks, based on focused ion beam (FIB) analysis. Further, Arkush et al.<sup>4</sup> and Moreno et al.<sup>12</sup> have observed hydride corrosion at twin and grain boundaries using scanning electron microscopy (SEM). Atomic force microscopy (AFM) has been employed by Balooch and Hamza<sup>16</sup> to directly observe UH<sub>3</sub> growth at grain boundaries. Based on the above findings, it has been universally concluded that some particular positions on or in the U near-surface region can be investigated as initial nucleation sites, with the aim of determining the hydriding characteristics. Previous results<sup>11,17–19</sup> also indicate that hydride nucleates at the  $\alpha$ -U-U<sub>2</sub>Ti boundary, and that H reacts preferentially with  $\alpha$ -U. With regards to the nucleation and growth stage, Hill et al.<sup>13</sup> and Scott et al.<sup>20</sup> have found the phenomenon of hydride expansion in a particular direction (i.e., twinning). Further, the authors of this article have discovered that this hydride expansion occurs preferentially towards the metal bulk or surface (work unpublished).

The U hydriding could be divided several stages as mentioned above, and until now, the controlling factors for hydride pitting sites in the initial stage are still the key points of related study. However, relatively less attention was given on the hydride growth stage except for the reaction kinetic studies. In fact, how

<sup>1</sup>Institute of Materials Research, China Academy of Engineering Physics, 621900 Mianyang, China and <sup>2</sup>Science and Technology on Surface Physics and Chemistry Laboratory, P.O. Box Nos. 9–35, Huafengxincun, 621908 Jiangyou City, China  
Correspondence: Peng Shi (shipeng@caep.cn) or Xiaolin Wang (xlwang@caep.cn)

Received: 18 September 2018 Accepted: 1 February 2019

Published online: 26 February 2019

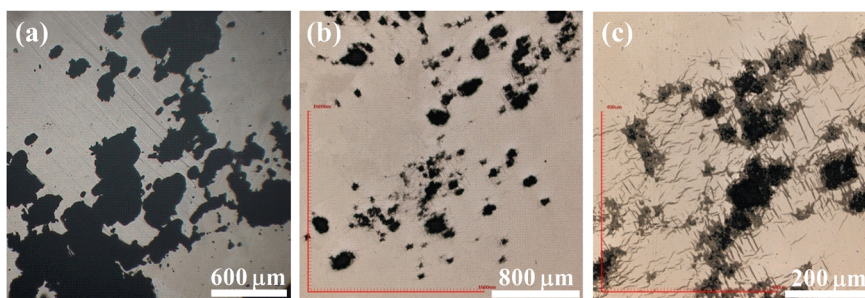


**Fig. 1** Laser scanning confocal microscope (LSCM) photographs of uranium (U) surface **a** after hydriding and **b, c** after slight surface polishing

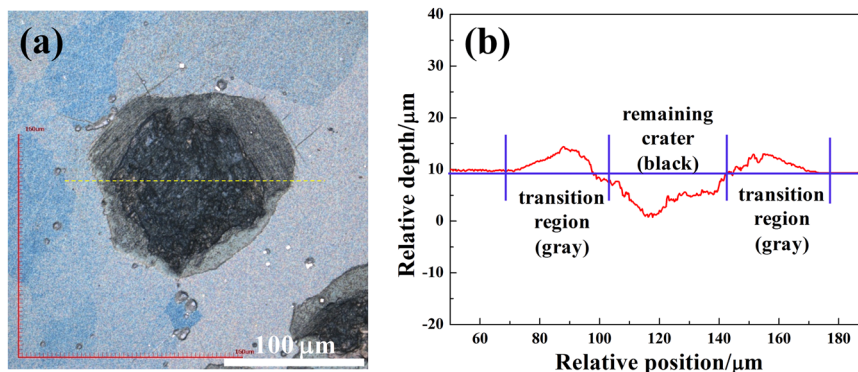


**Fig. 2** **a** Laser scanning confocal microscope (LSCM) photograph of a hydride crater. **b** Plot corresponding to the yellow line of the same crater

the reaction front extends during the dynamic reaction procedure strongly affect the corrosion behavior including the crater shape, which is an important factor for material performance. With regard to a hydride crater (surface oxide layer being broken up), hydrogen may firstly diffuse and distribute in the bulk near crater edge, once the H concentration reaches the critical value in particular sites, phase transformation happens and reaction propagates. The internal metal microstructure characteristics may play a vital role in the hydride growth.

In this work, U hydriding experiments are performed with focus on the H attacking regions beneath the hydride craters. A strain transition region was found in the vicinity of the crater edge. Time-of-flight secondary ion mass spectroscopy (TOF-SIMS) and X-ray photoelectron spectroscopy (XPS) are utilized to examine the transition regions beneath the hydride craters. The existence of a micro-scale induction period, which is different from the starting induction period, before  $\text{UH}_3$  phase transformation during the hydriding growth procedure is also deduced. Within this induction period, the H atoms diffuse and accumulate at some particular sites before reaching the critical concentration required to form stoichiometric  $\text{UH}_3$ .

## RESULTS

A number of hydride sites could be observed after hydriding experiments, these hydride sites grew in a specific direction or simply stochastically alongside the craters, as shown in Fig. 1a. This photograph illustrates the hydride expansion, focusing on the sample surface. To reveal the under-surface information, the post-hydriding sample was then abraded and polished slightly layer by layer. The corresponding results after approximately 5  $\mu\text{m}$  are shown in Fig. 1b, c, in which the black features are hydride craters that were not fully abraded. The bulk material could also be distinguished by the color difference. It can be seen that, each black crater is surrounded by a large number of line-type or plate-

like gray transition regions, which lie between the black craters. Figure 2b shows a cross-section outline corresponding to the yellow line in Fig. 2a, located on the crater center. In the Fig. 2b plot, material above the blue line was removed by the polishing process. The remaining transition regions and shallow crater are distributed on the pre-crater position. Further, line-type or plate-like gray cracks are distributed in the transition region (Fig. 1c). H atoms had diffused into these cracks, which can be easily distinguished by their gray color, since the craters are black and the bulk color is lighter.

The cross-section morphology of the hydride craters was acquired by polishing the reaction sample in the direction perpendicular to the reaction surface. Figure 3 illustrates the cross-section morphology of one hydride crater. From Fig. 3a, we can see that the hydrogen attacked region shows a semi-elliptical shape. A number of line-type gray cracks could be observed near the reaction front, this is identical to the surface morphology around the large hydriding craters, as shown in Fig. 1c.

These line-type gray cracks are possibly related with the transformation twinning region. First, regardless of the degree of surface polishing and cross-section abrasion, the line-type gray cracks are always present in or adjacent to the hydride craters. Further, the color discrimination between the bulk and these regions must be attributed to the H action on these regions. Second, a previous EBSD study reported extensive twinning within the metal grains in the vicinity of hydride craters.<sup>7</sup> It is believed that transformation twinning occurred in that case because of the generation and accumulation of internal stress during the reaction, accompanied by volume expansion due to the hydride formation.<sup>7,21</sup> EBSD analyses have proven that twinning in U occurs at nucleation sites, and hydride grows in conjunction with twinning.<sup>5,13</sup> Under these conditions, the twinning may act as a kind of diffusion channel and H may congregate in these internal channels beneath the hydride craters. However, in the examined samples, the H concentration had not reached the critical

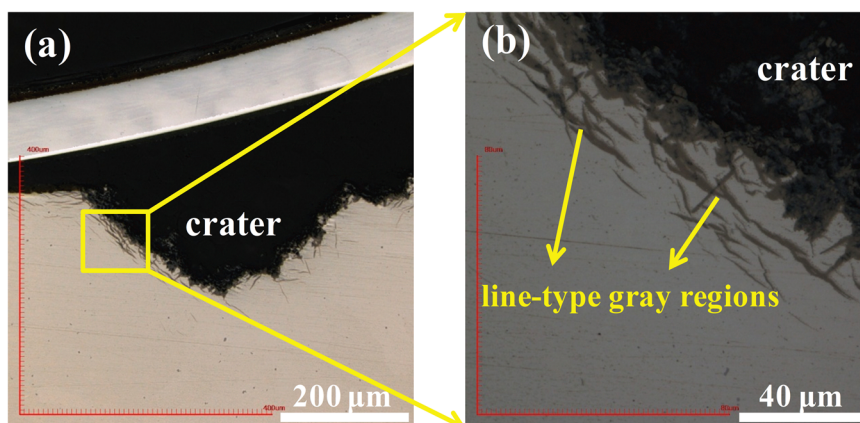


**Fig. 3** **a** Laser scanning confocal microscope (LSCM) photograph focusing on a well-polished mechanically sectioned hydride crater and **b** a locally magnified photograph focusing on the transition region

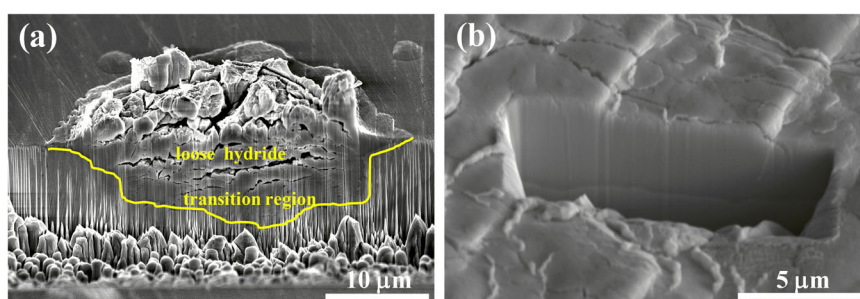


**Fig. 4** **a** Scanning electron microscopy (SEM) images of cross-section cut through hydride pit. The hydride is clearly distinguished by the loose material. There is an obvious boundary between the hydride and bulk uranium (U), indicated by the contrast difference. **b** SEM image of cross-section cut through a hydrided region, there is an obvious boundary between hydride and bulk U

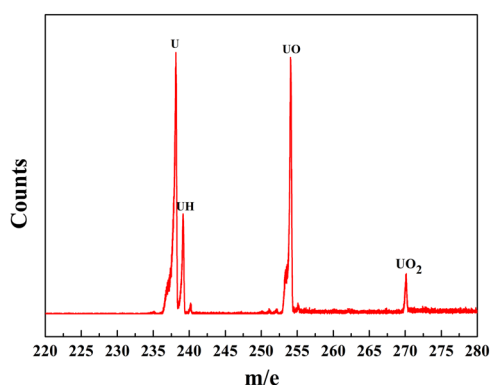


**Fig. 5** Secondary ion mass spectrum of hydriding region after polishing and  $\text{Au}^+$  sputter cleaning for 5 min

concentration required to cause phase transformation for  $\text{UH}_3$  formation.<sup>9</sup>

Furthermore, the cross-sections of the reacted regions on the micro-scale were acquired via FIB, as shown in Fig. 4. Figure 4a shows the cross-section of a smaller hydride crater and Fig. 4b shows a H-damaged area where the surface oxide layer had not cracked. The obvious contrast differences in the SEM photographs indicate the H activity regions. The regions between the loose hydride or surface layer and the bulk are the so-called transition regions.

The H distribution in the so-called transition regions was analyzed using TOF-SIMS, as described in the third paragraph of the Methods section. Figure 5 shows the different clustered ion contents, the  $\text{U}^+$  and  $\text{UO}^+$  ions had the strongest intensity,

whereas the  $\text{UH}^+$  and  $\text{UO}_2^+$  ion intensities were relatively weak. This clearly indicated that H atoms were detected in the target area on the reaction sample surface after the processing described above. Figure 6 shows SE (secondary electron) and SIMS images of a  $200\ \mu\text{m} \times 200\ \mu\text{m}$  region of hydrogenated U metal, focusing on a hydride crater with a slightly abraded surface. Figure 6a–d are an SE image and secondary ion  $\text{UO}^+$ ,  $\text{UH}^+$ , and  $\text{UO}_2^+$  images, respectively. In the four photographs, the hydride crater is distinguished by color difference, being notably darker. In the previous section, the transition region was distinguished by line-type and plate-like gray regions. From comparison of the similar regions in Fig. 6b, c, bright regions are visible around the dark craters. This implies higher H and O content in those regions than in the bulk; in other words, H was present in the transition regions. From Fig. 1 and 3a, it can be deduced that the line-type and plate-like regions formed as a result of the diffusion of H. However, in the secondary ion  $\text{UH}^+$  image (Fig. 6c), the H-diffused regions around the craters can be clearly distinguished relative to the bulk. Thus, these regions can be identified as transition regions. However, it should be noted that the gray line-type and plate-like regions must have some differences from the transition field. Further, the O and H enrichment fields have almost identical location, which indicates that the fields into which the H diffused had poorer corrosion resistance to O when subjected to wet abrasion and polishing.

The surface potential on a H-damaged area of  $0.8\ \text{mm} \times 0.8\ \text{mm}$  was acquired by the SKP (scanning Kelvin probe) system, as shown in Fig. 7. Before SKP analysis, the hydriding sample surface had been polished slightly to remove the loose material caused by volume expansion and to reveal the so-called transition regions. In Fig. 7, the surface potential fluctuations are obvious, the maximum potential contrast was approximately 400 mV, which is sufficient

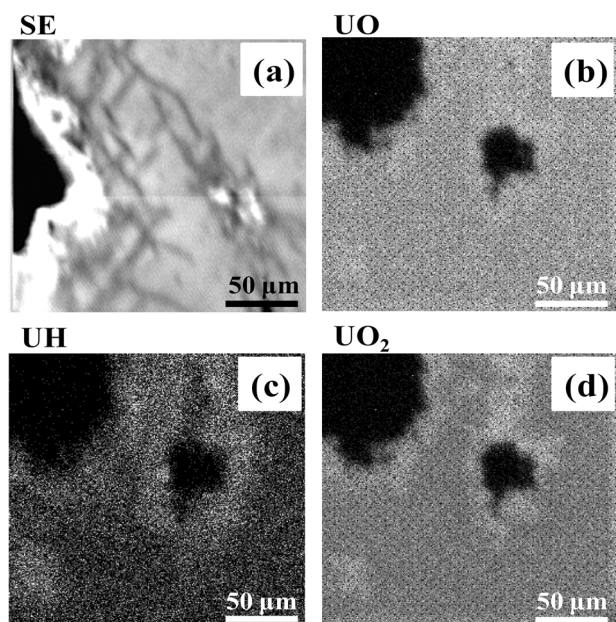


**Fig. 6** **a** SE image of 200 μm × 200 μm region focusing on hydriding craters of reacted sample after polishing. **b–d** Secondary ion mass spectroscopy (SIMS) images for UO<sup>+</sup>, UH<sup>+</sup>, and UO<sub>2</sub><sup>+</sup>

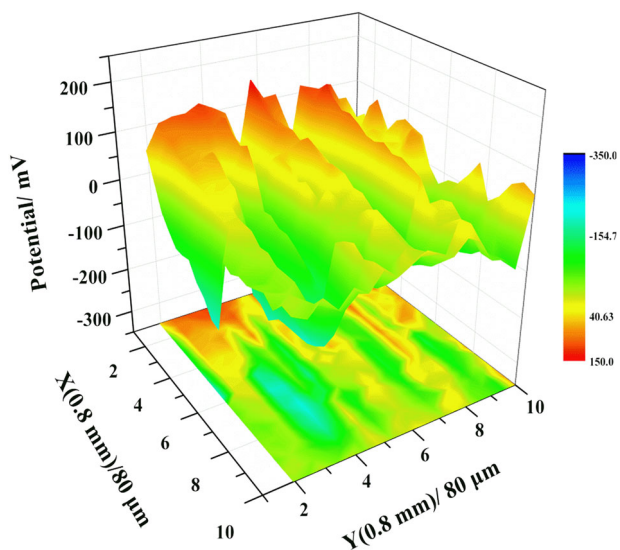


**Fig. 7** SKP 3D-potential image of well-polished hydrided uranium (U)

to distinguish different regions by the surface potential distribution. Greater corrosion occurs in a lower-potential area<sup>19,22–25</sup>; thus, the fluctuating surface potentials indicate areas with different levels of corrosion resistance. From Fig. 7, we can deduce that, first, during the hydriding reaction, the formation of UH<sub>3</sub> craters caused stress field and plastic deformation, leading to the easy diffusion of H into these regions along certain transition path, which rendered these areas susceptible to be attacked by the subsequent H. Second, after hydriding and during the polishing process, these areas also exhibited poor corrosion resistance to H, as confirmed by the secondary ion images in Fig. 6. Therefore, considering the surface potential fluctuation, the perfect surface had the highest potential, the transition region had lower potential, whereas the craters corresponded to the lowest-potential region because of the missing material.

High-resolution X-ray photoelectron spectra of O1s and U4f for the transition regions are shown in Fig. 8a, b, respectively. Prior to spectrum acquisition, sputter cleaning was performed for pure U without hydriding for 10 min, so as to obtain a clean U surface. Then, the spectra corresponding to the clean U surface were obtained for the parameters discussed in the fifth paragraph of the Methods section. Next, the spectrum acquisition operation was applied to a hydriding sample with a surface that was slightly polished to reveal the similar transition areas. Focusing on a transition region near a large hydride crater, a series of high-resolution XPS spectra were obtained for the surface in a step-by-step manner, from non-sputtered to 5-min sputtering, and then to 10-min sputtering. XPS spectra collected from a sputtering-cleaned U specimen were used as reference. For the hydriding sample, the U4f-oxide signals in Fig. 8 exhibit an obvious tendency to shift toward a higher binding energy (BE) as the sputtering progressed. In addition, single low-intensity satellites positioned at 6.5 and 6.8 eV to the high-BE side of U4f7/2 are apparent for the hydriding sample before and after sputtering, respectively. These results are in agreement with those of Pireaux et al.<sup>26</sup> and Allen et al.<sup>27</sup> who reported that the UO<sub>2</sub> surface possesses satellite structures observed at 6.4 and 8.2 eV, respectively. In the transition area, the U4f7/2 peak increases to 381.4 eV, due to H<sup>+</sup> cation bind the oxyanion together, which agreed with a reported result.<sup>28</sup>

Differences before and after sputtering are apparent for the O1s peaks, in terms of the peak positions and shapes. The O1s peak shifted to a higher BE after the sputtering process. From the U4f peak discussed above, the component corresponding to the three O1s-U peaks was determined to be UO<sub>2</sub>. Note that a O1s-H peak positioned at 532.2 eV could be clearly observed for the non-sputtered surface. After sputtering, O1s-H peaks positioned at 531.8 eV were discovered through peak assignment using XPS Peak 4.1 Software, as shown in Fig. 9. These peaks shifted slightly to a higher BE. These results prove the presence of H atoms located in the transformation regions, from a different approach. In addition, the data are in good agreement with those acquired from the SIMS analysis.

The relative sensitivity factor method was applied to calculate the O/U concentration ratios for each situation, where

$$C_{\text{O}}/C_{\text{U}} = I_{\text{O}}/S_{\text{O}}/I_{\text{U}}/S_{\text{U}}. \quad (1)$$

Here,  $C$  is the concentration of each element,  $I$  is the corresponding peak intensity, and  $S$  is the relative sensitivity factor for each element. The O/U concentration ratios for the transformation regions of the hydriding sample before and after 5-min and 10-min sputtering were 2.03, 1.93, and 1.85, respectively, as determined using Eq. (1). Then, the oxidized product was proven to be UO<sub>2</sub>. From observation of the transformation areas combined with the secondary ion image for UO<sub>2</sub>, it seems that oxidation to form UO<sub>2</sub> occurred more easily in these transition regions than in the other parts. However, although the ratios obtained here are the approximate values for the O and U element concentrations, they still indicate a tendency for the O-element relative concentration to decrease as the detection progressed further into the bulk. This implies that the presence of the H element may facilitate easy oxidation of the area to form UO<sub>2</sub>. Note that, in the presence of U-hydroxide, a similar result can be found for an Al alloy surface.<sup>29</sup>

## DISCUSSION

The U-sample surface was reacted by H, forming a number of hydride blisters and, subsequently, hydride craters. In previous studies, it was concluded that this reaction initially occurs on the oxide and U interface, and progresses with propagation of the reaction front. Jones et al. have reported the occurrence of subtle grain deformation in the vicinity of the reaction front.<sup>7</sup> However, the results of the present work indicate that the reaction front is

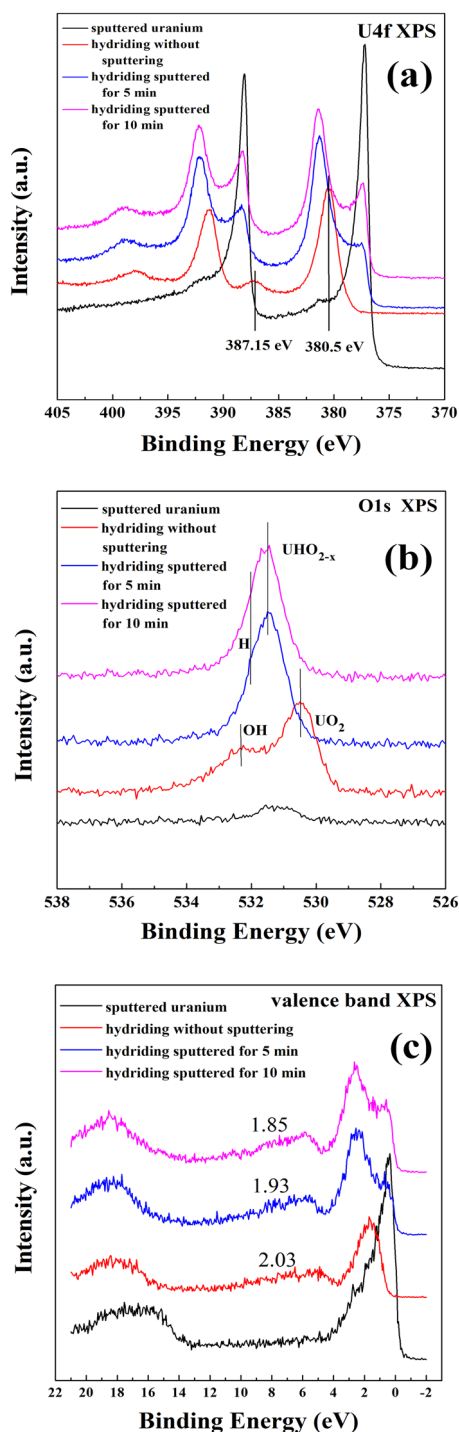


**Fig. 8** **a** U4f, **b** O1s, and **c** valence band X-ray photoelectron spectroscopy (XPS) spectra of sample surface

not simply an obvious interface between the bulk material and the loose or powder product. Instead, there exists a strain field transition area with a certain thickness, and H diffuses easier into it along certain diffusion path such as twinning. Detailed discussion of the findings is presented in the subsequent sections.

The surface polishing and cross-section polishing morphologies of the hydride craters revealed gray areas in the vicinity of the loose craters for both the surface-polished (Fig. 1) and cross-section-polished samples (Fig. 3). Further, severe H acted appearance was observed on the dark gray lines among these

gray areas. Because the dissolved H concentration required to form stoichiometric  $\text{UH}_3$  throughout some of the areas had not been reached,<sup>9</sup> the H atoms just diffused into those areas, but hydride powder did not form. Under those conditions, the corrosion resistance in the areas is relatively weak compared with the metal bulk, as proved by the SKP results, which illustrated that the surface potential values of those areas lay between those for the bulk material and craters.

TOF-SIMS and XPS were applied to investigate the presence and existence form of H in the transition areas of the reacted surface after slight polishing. The SIMS results indicate the presence of the H element as strong  $\text{UH}^+$  peak and weak  $\text{UH}_2^+$ , and the corresponding secondary ion  $\text{UH}^+$  image exhibits that H distributed in these transition regions with fine correspondence with the gray line-type distributed areas. And the XPS BE shifting of U4f indicated the presence of the  $\text{H}^+$  cation. On the other hand, the O1s BE for the transition field implies an O-H covalence contribution to the spectra. The H element diffused into the bulk before the reaction front during hydriding. In addition, for the region shown in the secondary ion  $\text{UO}_2^+$  image (Fig. 6d), similar bright areas to those of the secondary ion  $\text{UH}^+$  image (Fig. 6c) were observed, indicating more significant oxide corrosion in those areas than in the metal bulk. That is, the H diffused into and dispersed within the material bulk, weakening the corrosion resistance of these fields to O and even water. Note that U oxidation occurs extremely easily, even in an XPS high-vacuum chamber of  $10^{-9}$  mbar let alone the hydriding reaction chamber with the vacuum of  $10^{-4}$  mbar. Therefore, the obtained surface information always included  $\text{UO}_2$  or some other oxide. If it is assumed that the hydriding reaction and surface sputtering was performed under extreme O-free conditions with sufficient sputtering depth, the detection results may merely indicate U and H. At those locations, the H occupied special sites, such as dislocations, grain boundaries, and twinning boundaries, or combined with metallic U.<sup>30,31</sup> Note that H may interact with U to form UH or a  $\text{UH}_2$  cluster.

At last, based on the analysis and discussion about the transition region above, a micro-scale induction period model could be developed as illustrated by a hypothetical schematic diagram shown in Fig. 10. This is an attempt to propose a reaction model that briefly describes the hydride crater nucleation and growth, and the role played by the transition regions. The micro-scale induction period here refers to a period that starts at the moment when hydrogen atoms segregate in some special places, after that, the hydrogen number density increases. When the hydrogen concentration reaches the critical concentration, the phase transformation to  $\text{UH}_3$  will happen, and this is the end of the micro-scale induction period. We focused on the cross-section of a hydride crater in Fig. 10. First, hydride nucleates in a special site, which may be an inclusion or boundary, after an initial induction period. Second, as the reaction continues, the nucleation site grows in conjunction with the propagation of the reaction front and the volume expansion. The material in the vicinity of the craters suffers a strain field caused by volume expansion. Hence, the H diffuses easily into the internal material beyond the reaction front along special channels, such as the pre-existing twinning or grain boundaries (corresponding to the line-type or plate-like parts) to form a transition region. Further, as the volume expansion distorts the regions near the edge of a hydride crater, some strain can accumulate; this strain may also play an active role in H diffusion into the bulk. If particular sites such as defects, impurities, or defaults are located on the diffusion channel, the local energy is lower<sup>32,33</sup> and H is likely to accumulate in these sites. Once the H content reaches the critical concentration required to form stoichiometric  $\text{UH}_3$ , phase transformation may occur for  $\text{UH}_3$  formation. In fact, this process happened on those micro-scale sites is similar to that happened in the hydriding induction period stage. In this way, we can call this process to be a

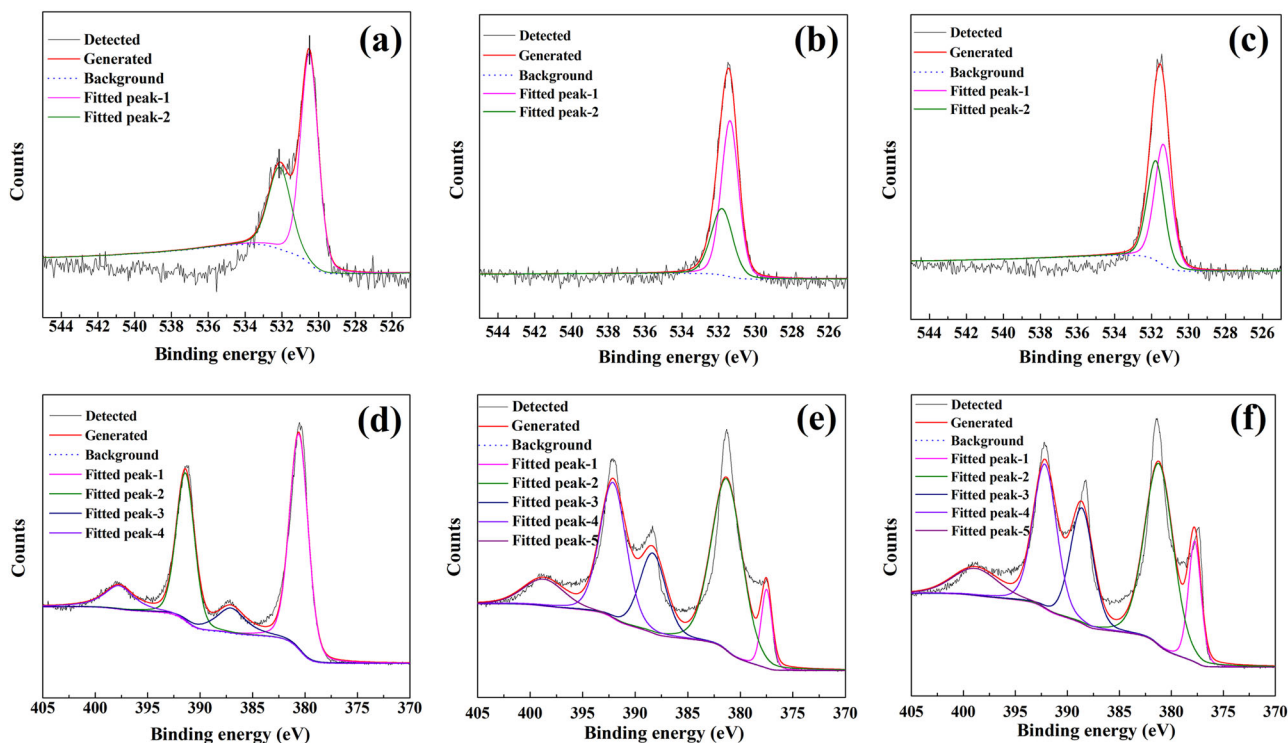


**Fig. 9** Fitting spectra for **a** O1s of hydriding sample before sputtering, **b** O1s of hydriding sample sputtered for 5 min, **c** O1s of hydriding sample sputtered for 10 min, **d** U4f of hydriding sample before sputtering, **e** U4f of hydriding sample sputtered for 5 min and **f** U4f of hydriding sample sputtered for 10 min

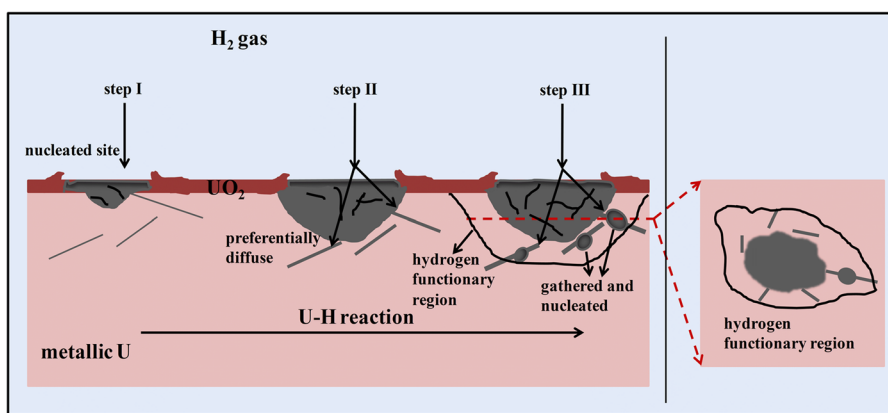


**Fig. 10** Hypothetical schematic diagram illustrating existence and formation of supposed transition region

micro-scale induction period. As the attack proceeds, the material go through thousands of the so-called micro-scale induction periods successively, behaving the continuous reaction on the macro-scale level. The whole process is dynamic, if H content has not reach the critical concentration, it dispersed within the region, which is regarded as a transition region. So the transition regions around main hydride crater may be composed of hydride streamers, hydrogen-rich regions and unreacted U. The transition regions observed in this work were distributed three-dimensionally, had limited thickness, and were in the vicinity of the crater edge. The sketch map of a crater polished parallel to the reaction surface is shown on the right side of Fig. 10 to reveal a transition region also surrounding the crater.

To conclude, this study explored U–H interaction beneath hydride craters and defined regions of limited thickness as transition regions between the hydride reaction product and U bulk into which the H diffused. The obtained laser scanning

confocal microscope (LSCM) photographs of surface-polished and cross-section-polished craters provide morphological proof of the existence of the transition regions. The existence of transition regions in the vicinity of the hydride craters reveals that it is not an obvious interface but a region with a certain thickness between the bulk U and loose hydride. Further, the SKP results indicate that the transition regions have poorer corrosion resistance than the fine surface. The SIMS results confirm that H is dispersed in the transition regions, and that there is also O distribution in the same regions. Combined with the XPS investigation, H exists covalently with U and oxygen in these transition regions. Above all, as in the initial stage of hydriding with respect to surface nucleation, aiming at the hydride growth, a micro-scale induction period model could be proposed to further understand the U hydriding reaction mechanism. Within these micro-scale induction periods, the H diffuses and accumulates in particular sites before reaching

the critical concentration for formation of stoichiometric  $\text{UH}_3$ , and hydride grows or expands into the bulk or along the surface.

## METHODS

Before the hydriding experiment, U sample was prepared in the open laboratory. The hydriding experiment itself was conducted in a hot-stage microscope system equipped with a sealed furnace chamber having a quartz glass window. Details of the experimental procedure are described elsewhere.<sup>19</sup> The chamber was heated to 160 °C under dynamic vacuum for 1 h for corrosion acceleration, so as to acquire H-attacked areas in a relatively short time.<sup>34</sup>

The post-hydriding U-sample surface morphology was acquired using a LSCM. The attacked surface was slightly polished using 4000-grit SiC paper and subsequently, the samples were wet polished by standard mechanical techniques using 2.5  $\mu\text{m}$  diamond abrasive on a low-nap cloth with water vehicles. The detailed information of the damaged regions was observed. In addition, large-scale section polishing was also performed, focusing on the hydride funnel-like pits; hence, the growth characteristics of the hydride craters in the metal base could be acquired by image reconstruction. Furthermore, the detailed information on the micro-scale of selected hydride pits was obtained using an FIB (FEI FIB-model). To obtain high-resolution secondary electron images, the images were taken at 53° to the cut face and captured using a current beam (2.8 nA).

TOF-SIMS, as an advanced method for surface analysis of solid specimens, has remarkably high spatial and mass resolutions, as well as high sensitivity for elemental and isotopic measurements over a wide mass range. TOF-SIMS was used to analyze U and hydrogen-related mass fragments distribution after hydriding. A 25-keV liquid metal ion gun was used for analysis and as a sputtering gun, if provided pulsed (analytical mode) and focused (sputtering mode) primary ion beams, respectively. The beam energy ranged from 10 to 25 kV, with a minimum spot size of 200 nm at 25 kV in pulsed (analytical) mode for  $^{197}\text{Au}^+$ . A background pressure of  $1 \times 10^{-9}$  mbar was maintained to prevent surface oxidation during the experimental process. The samples were slightly mechanically polished as mentioned above. Before the measurement, the surface was sputtered to depths of 1–20 nm through  $\text{Au}^+$  sputter ion beam scanning over 1500–2000  $\mu\text{m}$ , to remove the oxide layer and obtain a clear surface.  $\text{UO}^+$ ,  $\text{UO}_2^+$ , and  $\text{UH}^+$ -positive ions and images were also acquired using 25 kV  $\text{Au}^+$  ions with currents between 1.5 and 2 pA.

SKP analysis of the hydriding sample surface subjected to slight polishing was performed using a SKP 5050 system (KP Technology). A scan area of 0.8 mm  $\times$  0.8 mm was selected on the H-damaged region on the slightly polished surface. The surface potential distributions corresponding to the H-damaged and unattacked surfaces were acquired to explore the influence of H on the surface potential of the U surface.

XPS (ESCALAB 250) analysis was performed using a monochromatic AlKa ( $h\nu = 1486.68$  eV, 150 W) X-ray source (analysis area diameter: 500  $\mu\text{m}$ ) with 20-eV pass energy for a high-resolution scan. Sputter cleaning was performed by sputtering the specimens for 5 min with scanning argon (Ar)-ion gun operating at 2-keV ion energy with a 2 mm  $\times$  2 mm scan size. For the U samples reacted with H, the spectra were first acquired for a non-sputtered surface. Then, after ion-sputtering for 5 and 10 min, the corresponding XPS spectra were acquired. In addition, a pure U specimen with no H reaction was introduced to the analysis chamber to provide a series of pure metal spectra. Sputter cleaning of the metal surface was performed before spectrum acquisition.

## DATA AVAILABILITY

The datasets generated during and/or analyzed during the current study are all available from the corresponding authors on request.

## ACKNOWLEDGEMENTS

This work was supported by the National Natural Science Foundation of China [grant number 51701195]. The authors would like to thank Xian'e Tang and Li Zhang for their help and guidance with sample preparation, and Chao Lu for his assistance with sample surface processing.

## AUTHOR CONTRIBUTIONS

X.W. and P.S. supervised the study. H.J. was responsible for experimental analysis and wrote the paper. H.W., Q.P., D.C., and X.M. performed the TOF-SIMS, XPS, SKP, and FIB analyses, respectively. X.C. was involved in data interpretation.

## ADDITIONAL INFORMATION

**Supplementary information** accompanies the paper on the *npj Materials Degradation* website (<https://doi.org/10.1038/s41529-019-0073-6>).

**Competing interests:** The authors declare no competing interests.

**Publisher's note:** Springer Nature remains neutral with regard to jurisdictional claims in published maps and institutional affiliations.

## REFERENCES

- Banos, A., Jones, C. P. & Scott, T. B. The effect of work-hardening and thermal annealing on the early stages of the uranium-hydrogen corrosion reaction. *Corros. Sci.* **131**, 147–155 (2018).
- Banos, A., Harker, N. & Scott, T. B. A review of uranium corrosion by hydrogen and the formation of uranium hydride. *Corros. Sci.* **136**, 129–147 (2018).
- Owen, L. W. & Scudamore, R. A. A microscope study of the initiation of hydrogen-uranium reaction. *Corros. Sci.* **6**, 461–465 (1966).
- Arkush, R. et al. Site related nucleation and growth of hydrides on uranium surfaces. *J. Alloy. Compd.* **244**, 197–205 (1996).
- Bingert, J. F. Jr., R. J. H., Field, R. D. & Dickerson, P. O. Microtextural investigation of hydrided  $\alpha$ -uranium. *J. Alloy. Compd.* **365**, 138–148 (2004).
- Jones, C. P., Scott, T. B., Petherbridge, J. R. & Glascott, J. A surface science study of the initial stages of hydrogen corrosion on uranium metal and the role played by grain microstructure. *Solid State Ion.* **231**, 81–86 (2013).
- Jones, C. P., Scott, T. B. & Petherbridge, J. R. Structural deformation of metallic uranium surrounding hydride growth sites. *Corros. Sci.* **96**, 144–151 (2015).
- Lide, D. R. & Haynes, W. M. *CRC Handbook of Chemistry and Physics* 90th edn, 2804 (CRC Press, Boca Raton, FL, 2009).
- Loui, A. *The Hydrogen Corrosion of Uranium: Identification of Underlying Causes and Proposed Mitigation Strategies*. Report No. LLNL-TR-607653, (Lawrence Livermore National Lab (LLNL), Livermore, CA (United States), 2012).
- Musket, R. G., Robinson-Weis, G. & Patterson, R. G. Modification of the hydriding of uranium using ion implantation. *MRS Online Proceedings Library (OPL)* **27**, 753–758 (1983).
- Shi, P. et al. Effect of alloyed Ti on the microstructure and corrosion characteristics of a U-Ti alloy in a hydrogen environment. *Corros. Sci.* **93**, 58–62 (2015).
- Moreno, D., Arkush, R., Zalkind, S. & Shamir, N. Physical discontinuities in the surface microstructure of uranium alloys as preferred sites for hydrogen attack. *J. Nucl. Mater.* **230**, 181–186 (1996).
- Hill, M. A. et al. Filiform-mode hydride corrosion of uranium surfaces. *J. Nucl. Mater.* **442**, 106–115 (2013).
- Banos, A. & Scott, T. B. Statistical analysis of  $\text{UH}_3$  initiation using electron back-scattered diffraction (EBSD). *Solid State Ion.* **296**, 137–145 (2016).
- Harker, R. M. & Chohollo, A. H. Surface analytical study of uranium exposed to low pressures of hydrogen at  $\sim 80$  °C. *MRS Online Proceedings Library (OPL)* **1444**, 189–195 (2012).
- Balooch, M. & Hamza, A. V. Hydrogen and water vapor adsorption on and reaction with uranium. *J. Nucl. Mater.* **230**, 259–270 (1996).
- Ji, H. et al. The microstructure and hydriding characteristics of high temperature aged U-13 at.%Nb alloy. *J. Nucl. Mater.* **464**, 43–47 (2015).
- Shi, P. et al. Preferred hydride growth orientation of U-0.79wt.%Ti alloy with  $\beta + \text{U}_2\text{Ti}$  microstructure. *J. Nucl. Mater.* **441**, 1–5 (2013).
- Ji, H. et al. The effects of microstructure on the hydriding for 500 °C/2h aged U-13. at.%Nb alloy. *J. Nucl. Mater.* **488**, 252–260 (2017).
- Scott, T. B., Allen, G. C., Findlay, I. & Glascott, J.  $\text{UD}_3$  formation on uranium: evidence for grain boundary precipitation. *Philos. Mag.* **87**, 177–187 (2007).
- Taplin, D. M. R. On the question of the grain size dependence of the flow and fracture stress in alpha uranium. *J. Nucl. Mater.* **19**, 208–209 (1966).
- Sababi, M., Ejnermark, S., Andersson, J., Claesson, P. M. & Pan, J. Microstructure influence on corrosion behavior of a Fe-Cr-V-N tool alloy studied by SEM/EDS, scanning Kelvin force microscopy and electrochemical measurement. *Corros. Sci.* **66**, 153–159 (2013).
- Sathirachinda, N., Pettersson, R., Wessman, S. & Pan, J. Study of nobility of chromium nitrides in isothermally aged duplex stainless steels by using SKPFM and SEM/EDS. *Corros. Sci.* **52**, 179–186 (2010).
- Li, M., Guo, L. Q., Qiao, L. J. & Bai, Y. The mechanism of hydrogen-induced pitting corrosion in duplex stainless steel studied by SKPFM. *Corros. Sci.* **60**, 76–81 (2012).

25. Álvarez-Asencio, R. et al. Role of microstructure on corrosion initiation of an experimental tool alloy: a quantitative nanomechanical property mapping study. *Corros. Sci.* **89**, 236–241 (2014).
26. J.Pireaux, J., Riga, J., Thibaut, E., Tenret-Noël, C. & Caudano, R. et al. Shake-up satellites in the x-ray photoelectron spectra of uranium oxides and fluorides. A band structure scheme for uranium dioxide, UO<sub>2</sub>. *Chem. Phys.* **22**, 113–120 (1977).
27. Allen, G. C., Tucker, P. M. & Tyler, J. W. The behaviour of uranium oxides in low partial pressures of O<sub>2</sub> studied using X-ray photoelectron spectroscopy. *Vacuum* **32**, 481–486 (1982).
28. Ilton, E. S. & Bagus, P. S. XPS determination of uranium oxidation states. *Surf. Interface Anal.* **43**, 1549–1560 (2011).
29. Zähr, J., Oswald, S., Türpe, M., Ullrich, H. J. & Füssel, U. Characterisation of oxide and hydroxide layers on technical aluminum materials using XPS. *Vacuum* **86**, 1216–1219 (2012).
30. Lillard, R. S., Taylor, C. D., Wermer, J. R., Mara, N. A. & Cooley, J. C. A thermal desorption study of the kinetics of uranium hydride decomposition. *J. Nucl. Mater.* **444**, 49–55 (2014).
31. Lillard, R. S. & Forsyth, R. T. A thermal desorption spectroscopy study of hydrogen trapping in polycrystalline  $\alpha$ -uranium. *J. Nucl. Mater.* **461**, 341–349 (2015).
32. Christopher, D., Taylor, T. L. & Scott, L. Ab initio calculation of the uranium-hydrogen system: thermodynamics, hydrogen saturation of  $\alpha$ -U and phase-transformation to UH<sub>3</sub>. *Acta Mater.* **58**, 1045–1055 (2010).
33. Taylor, C. D. & Lillard, R. S. Ab-initio calculations of the hydrogen–uranium system: surface phenomena, absorption, transport and trapping. *Acta Mater.* **57**, 4707–4715 (2009).
34. Petherbridge, J. R., Knowles, J. & Bazley, S. G. The effect of thermal pre-treatments on the nucleation of uranium hydride. *Solid State Ion.* **292**, 110–115 (2016).



**Open Access** This article is licensed under a Creative Commons Attribution 4.0 International License, which permits use, sharing, adaptation, distribution and reproduction in any medium or format, as long as you give appropriate credit to the original author(s) and the source, provide a link to the Creative Commons license, and indicate if changes were made. The images or other third party material in this article are included in the article's Creative Commons license, unless indicated otherwise in a credit line to the material. If material is not included in the article's Creative Commons license and your intended use is not permitted by statutory regulation or exceeds the permitted use, you will need to obtain permission directly from the copyright holder. To view a copy of this license, visit <http://creativecommons.org/licenses/by/4.0/>.

© The Author(s) 2019